

Bubble Dynamics Transformer: Microrheology at Ultra-High Strain Rates

Lehu Bu (卜乐虎),¹ Zhaohan Yu,² Shaotong Lin (林少挺),² Jan N. Fuhr,¹ and Jin Yang (杨锦)^{1,3, a)}

¹⁾*Department of Aerospace Engineering and Engineering Mechanics, The University of Texas at Austin, Austin, TX, USA, 78712*

²⁾*Department of Mechanical Engineering, Michigan State University, East Lansing, MI, USA, 48824*

³⁾*Texas Materials Institute, The University of Texas at Austin, Austin, TX, USA, 78712*

(Dated: 16 June 2025)

Laser-induced inertial cavitation (LIC)—where microscale vapor bubbles nucleate due to a focused high-energy pulsed laser and then violently collapse under surrounding high local pressures—offers a unique opportunity to investigate soft biological material mechanics at extremely high strain rates ($> 10^3$ 1/s). Traditional rheological tools are often limited in these regimes by loading speed, resolution, or invasiveness. Here we introduce novel machine learning (ML)-based microrheological frameworks that leverage LIC to characterize the viscoelastic properties of biological materials at ultra-high strain rates. We utilize ultra-high-speed imaging to capture time-resolved bubble radius dynamics during LIC events in various soft viscoelastic materials. These bubble radius versus time measurements are then analyzed using a newly developed *Bubble Dynamics Transformer* (BDT), a neural network trained on physics-based simulation data. The BDT accurately infers material viscoelastic parameters, eliminating the need for iterative fitting or complex inversion processes. This enables fast, accurate, and non-contact characterization of soft materials under extreme loading conditions, with significant implications for biomedical applications and materials science.

Keywords: *Cavitation, Material characterization, Machine learning, Soft materials*

I. INTRODUCTION

The rheological characterization of soft materials at ultra-high strain rates ($> 10^3$ s $^{-1}$) is important for the understanding of their dynamic-mechanical behavior across a wide spectrum of engineering and biomedical applications. For instance, precise characterization of tissue properties during rapid loading is paramount for ensuring the safety and efficacy of laser and ultrasound-based surgical interventions, minimizing unwanted collateral damage¹. However, conventional techniques such as oscillatory shear plate rheometry², dynamic mechanical analysis (DMA)³, and micro- or nano-indentation^{4,5} often fall short when confronted with these extreme loading conditions, particularly those encountered in ballistic, ultra-high strain-rate regimes.

Recently, inertial microcavitation rheometry (IMR)^{6–10} has emerged as a promising and minimally invasive experimental technique to address this critical need. Specifically, IMR is designed for determining the nonlinear viscoelastic constitutive properties of soft materials at ultra-high strain rates ($> 10^3$ s $^{-1}$) by leveraging the physics and dynamics of inertial cavitation. By focusing a femtosecond- or nanosecond-duration laser pulse or a high-intensity ultrasound pulse within a transparent soft material, such as a liquid, hydrogel, elastomer, or biological tissue, IMR initiates a localized microscale cavitation bubble above a critical energy threshold. The subsequent rapid radial expansion and collapse of this bubble dynamically loads the surrounding material at ultra-high, ballistic strain rates, enabling localized and extreme-rate microrheological probing. Capturing the time evolution of the bubble dynamics, for example, the bubble radius R as a function of

time t , using ultra-high-speed imaging and comparing these experimental observations with theoretical simulations allows the quantification of the material's shear and loss moduli under these extreme loading conditions.

IMR has been demonstrated in characterizing a variety of viscous liquids¹⁰ and hydrogels, including polyacrylamide^{6,7}, agarose⁸, and gelatin¹³. Here, we aim to provide a concise review and synthesis of the previous advancements in IMR. Furthermore, despite the established success of IMR, its reliance on physics-based inverse models for parameter estimation often leads to significant computational costs. The current IMR methodology is also typically limited to two-parameter fitting, which can restrict its ability to accurately model more complex rheological behaviors. To overcome these limitations, this paper introduces a novel deep learning-based Transformer model¹⁴—*Bubble Dynamics Transformer* (BDT). This innovative approach promises near real-time rheology analysis and holds significant potential for expansion to multi-parameter fitting, thereby enabling the description of more intricate material responses.

II. METHODOLOGIES

A. Experimental Setup

Inertial microcavitation events – the foundation of IMR – can be induced through focused laser pulses (laser-induced cavitation, LIC) or ultrasound pulses (ultrasound-induced cavitation, UIC). To probe nonlinear viscoelastic properties at high strain rates, IMR leverages the violent collapse phase of inertial cavitation to load the surrounding material. It is crucial to recognize that the material experiences spatially and temporally varying, non-uniform strain rates and amplitudes under these conditions. Specifically, material near the bubble

^{a)}Electronic mail: jin.yang@austin.utexas.edu; Corresponding author

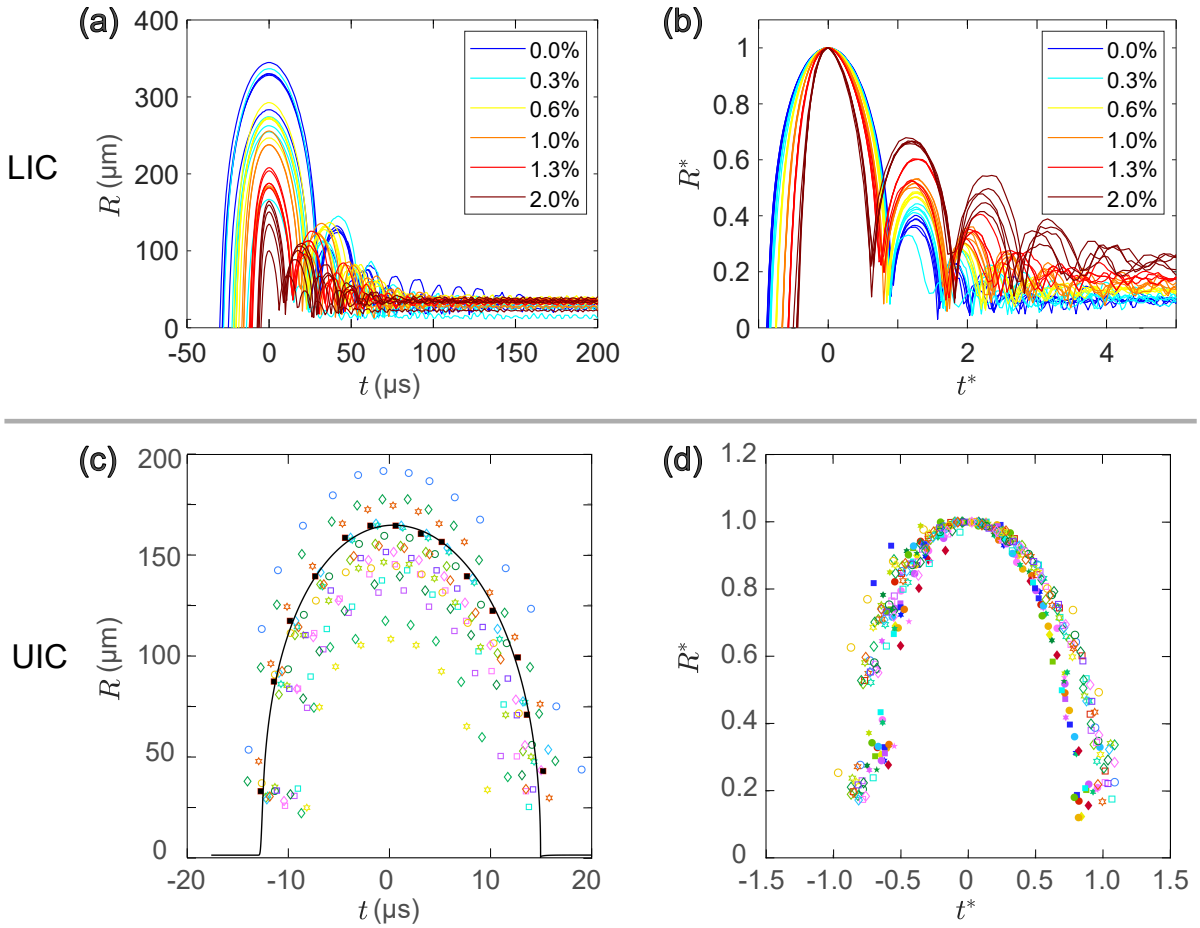


FIG. 1. (a) Dimensional radius R vs. time t curves for laser-induced inertial cavitation (LIC) experiments in “12 % PAAm + X%” alginate double network hydrogels (X% is the concentration of alginate which is labelled in the figure legend). (b) Nondimensionalized bubble radius R^* vs. time t^* curves for data in (a). (c) Dimensional radius R vs. time t curves for 19 ultrasound-induced inertial cavitation (UIC) experiments in 0.3 wt% agarose gel¹¹. The best fit simulation obtained with the neo-Hookean Kelvin-Voigt (NHKV) model (solid black line) is shown for a representative experimental data set (filled squares). (d) Scaled bubble radius vs. time data adapted from Wilson et al.¹² for 19 experiments in 0.3 wt% (open markers) agarose gel and 20 experiments in 1 wt% (filled markers) agarose gel.

wall undergoes very high strain rates but small strain values during bubble collapse. Conversely, these same regions experience larger strains at lower strain rates when the bubble reaches its maximum radius after the initial expansion. Both strain and strain rates progressively dampen as the bubble approaches its equilibrium radius. Regions further from the bubble wall consistently exhibit smaller strains and strain rates.

In this study, the reported strain rate is defined as the averaged strain rate from the point of the bubble’s maximum radius to its first violent collapse. Although cyclic ultrasound waves can induce bubble oscillations at a uniform frequency, achieving the high-strain and high-strain-rate regimes characteristic of IMR is more challenging with this method^{15,16}.

Laser-induced cavitation (LIC): In our LIC experiments, a single 6 ns pulse from an adjustable 125 mJ Q-switched Nd:YAG Minilite II (Continuum, Milpitas, CA) laser, frequency-doubled to 532 nm or 1064 nm, is focused

within the sample. The resulting cavitation bubble dynamics are recorded at frame rates of 110 million frames per second using ultra-high-speed cameras (Kirana5M, Specialized Imaging, Pitstone, United Kingdom; or HPV-X2, Shimadzu, Japan). Further experimental details can be found in Refs^{6,7}.

We chose polyacrylamide-alginate (PAAm-alginate) hydrogels¹⁷ as a model material to conduct LIC experiments. The experimental protocols of fabricating PAAm-alginate hydrogels are summarized in Lin et al.¹⁷. A PAAm-alginate hydrogel is made of two interpenetrating polymer networks: a covalently-crosslinked long-chain PAAm network and an ionically-crosslinked short-chain alginate network. The covalently-crosslinked long-chain PAAm network provides the material’s stretchable elasticity, and the ionically-crosslinked short-chain alginate network dissociates as the material is highly deformed, which can stiffen the overall hydrogel’s modulus and enhance its fracture toughness. Figure 1(a) presents the experimentally measured bubble R vs. t

curves conducted on double network hydrogels with varying alginate concentrations: “12 % PAAm + X%” alginate double network hydrogels (X is the concentration of alginate which is labeled in the figure legend.) The experimentally obtained R vs. t curves are further normalized and shown in Fig. 1(b) using the following formulas: $R^* = R/R_{\max}$; $t^* = t/t_c$. R_{\max} is the maximum bubble radius; t_c is defined as R_{\max}/U_c where $U_c = \sqrt{p_0/\rho}$; ρ is surrounding material mass density ($\rho \sim 1,000 \text{ kg/m}^3$); p_0 is the far-field ambient pressure ($p_0 \sim 101,325 \text{ Pa}$).

Ultrasound-induced cavitation(UIC): Besides using LIC, ultrasound-induced cavitation (UIC) can also be utilized to measure microrheology of the surrounding material viscoelastic properties at ultra-high strain rates¹¹. Experiments were performed in a water-filled, open-topped, spherical acoustic array that was 10 cm in diameter and populated with 16 focused transducer elements with a center frequency of 1 MHz. Single spherical bubbles were nucleated in the gel samples using a 1.5-cycle acoustic pulse containing a single rarefactional pressure half-cycle¹⁸ with an amplitude of -24 MPa . All cavitation events in this study were initiated solely by acoustic forcing¹⁹ – that is to say, no modifications (e.g., point defects or microbubble inclusions) were made to the gels in order to seed cavitation generation.

The bubbles were imaged through a single cycle of growth and collapse using a camera with a fixed frame rate of 400 kHz. The multi-flash-per-camera-exposure technique²⁰ generated images of nested, concentric bubbles, which were differentiated using brightness thresholding and edge detection. Bubble radii were measured at individual flash points by applying a circle fit to their detected boundaries. For all experiments, the magnitude of the spatial resolution uncertainty was less than $4.3 \mu\text{m}$, and the temporal resolution uncertainty was less than $1.25 \mu\text{s}$.

Dimensional radius R vs. time t curves for 19 ultrasound-induced inertial cavitation (UIC) experiments in 0.3 wt% agarose gel are shown in Fig. 1(c). Their non-dimensional curves are plotted in Fig. 1(d) adapted from Wilson et al.¹² for 19 experiments in 0.3 wt% (open markers) agarose gel and 20 experiments in 1 wt% (filled markers) agarose gel.

Inertial cavitation can either be induced by pulsed-laser or pulsed-ultrasound methods. The resultant bubble dynamics are demonstrably sensitive to the properties of the surrounding material, which will be detailed in Section II B, “Theoretical Modeling.” By integrating experimental data with a computational framework, this approach enables the extraction of microrheological material properties at ultra-high strain rates.

B. Theoretical Modeling of Microrheology at High Strain Rates

We model laser or ultrasound pulse-induced cavitation bubble dynamics using the modified Keller-Miksis equation^{6,7,21,22}. In this equation, the surrounding material is assumed to be hyperelastic and incompressible in the near

field, but it also accounts for the slight compressibility of the near field surrounding material by incorporating the material’s finite longitudinal wave speed c into the description of the far field. This yields the following modified evolution equation for the bubble radius $R(t)$:

$$\begin{aligned} \left(1 - \frac{\dot{R}}{c}\right) R \ddot{R} + \frac{3}{2} \left(1 - \frac{\dot{R}}{3c}\right) R^2 \\ = \frac{1}{\rho} \left(1 + \frac{\dot{R}}{c}\right) \left(p_b - p_\infty - p_f - \frac{2\gamma}{R} + S\right) \quad (1) \\ + \frac{1}{\rho} \frac{R}{c} \overline{\left(p_b - p_f - \frac{2\gamma}{R} + S\right)}, \end{aligned}$$

where ρ is the mass density of the surrounding soft material, which is assumed to be constant; γ is the surface tension of the bubble interface. “ $\overline{\bullet}$ ” denotes the time derivative of variable \bullet . S represents the pressure contribution due to the stress field in the surrounding hyper-viscoelastic material, which is given by

$$S = \int_R^\infty \frac{2}{r} (\sigma_{rr} - \sigma_{\theta\theta}) dr. \quad (2)$$

σ_{rr} and $\sigma_{\theta\theta}$ are the radial and circumferential components of the total Cauchy stress tensor σ in the surrounding material. If we model the surrounding material as a Kelvin-Voigt-type viscoelastic material^{6,23} where a hyperelastic spring branch is in parallel with a linear viscosity dash-pot, and assume the surrounding material is incompressible, the stress integral can be calculated analytically as⁷

$$\begin{aligned} S = \frac{(3\alpha - 1)G}{2} \left[5 - \left(\frac{R_0}{R}\right)^4 - \frac{4R_0}{R} \right] - \frac{4\mu\dot{R}}{R} \\ + 2\alpha G \left[\frac{27}{40} + \frac{1}{8} \left(\frac{R_0}{R}\right)^8 + \frac{1}{5} \left(\frac{R_0}{R}\right)^5 + \left(\frac{R_0}{R}\right)^2 - \frac{2R}{R_0} \right]. \quad (3) \end{aligned}$$

Parameter μ is the viscosity coefficient; G is the shear modulus (or storage modulus for the elastic contribution in rheology). α is a non-dimensional index for describing strain stiffening effects. Both G and α appear in the assumed hyperelastic strain energy function of the form

$$W = \frac{G}{2} \left[(I_1 - 3) + \frac{\alpha}{2} (I_1 - 3)^2 \right], \quad (4)$$

where $I_1 = \text{tr}(\mathbf{C})$ is the first invariant of the right Cauchy-Green deformation tensor $\mathbf{C} = \mathbf{F}^\top \mathbf{F}$; \mathbf{F} is deformation gradient tensor. Note that when strain-stiffening is neglected ($\alpha = 0$), the stress integral reduces to a special case where the hyperelastic spring branch is a neo-Hookean material model²⁴, and the overall hyper-viscoelastic material model is called neo-Hookean Kelvin-Voigt (NHKV) model. However, for more rheologically complex constitutive models, closed-form, analytical expressions for the stress integral may not be obtainable, requiring numerical calculations.

The evolution of the time-dependent absolute pressure inside the bubble $p_b(t)$ is governed by the physics of the

bubble contents, which we assume to be a homobaric mixture of water vapor and non-condensable gas^{6,25–27}. The mathematical description of bubble contents and the resulting evolution equation for $p_b(t)$ are summarized in Appendix A.

Initial and boundary conditions. In this work, we only consider pulsed laser-induced cavitation (LIC). When simulating LIC, we initialize the numerical simulations at the point in time where the bubble has at its maximum radius ($R = R_{\max}$). This is done because the initial growth phase of the bubble involves laser breakdown of the liquid and its associated plasma physics, which is not accounted for in the cavitation modeling framework. When the bubble is at its maximum radius, we idealize the system as being in thermodynamic equilibrium with the surroundings, but not in mechanical equilibrium. The driving force for the subsequent cavitation dynamics is the gauge pressure inside the bubble modified by the Laplace pressure ($p_b - p_{\infty} - 2\gamma/R$), while in LIC, the far-field gauge pressure remains zero ($p_f = 0$). For Keller-Miksis-based numerical solutions, the bubble radius and velocity are initialized as $R(t = 0) = R_{\max}$ and $\dot{R}(t = 0) = 0$, respectively.

C. Bubble Dynamics Transformer (BDT) Model Architecture

To further speed up the fit of the rheology material properties, we develop a new deep learning model called *Bubble Dynamics Transformer* (BDT) designed for the direct characterization of soft material viscoelastic properties. The BDT is based on the transformer architecture¹⁴, which has the advantage of having no recurrent units, therefore requiring less training time than earlier recurrent neural architectures (RNNs) such as long short-term memory (LSTM)²⁸. The BDT predicts the shear modulus (also the material’s storage modulus) and viscosity (related to the material’s loss modulus) directly from the dynamic bubble radius versus time (R - t) curves observed during violent collapse.

All transformers have the same primary components: *i*) *Tokenizers*, which convert text or numerical data into tokens—each token is an integer to represent a character/data or a short segment of characters/data; *ii*) *An embedding layer*, which converts tokens and positions of tokens into vector representations; *iii*) *Transformer layers*, which include encoder layers and decoder layers; *iv*) *An un-embedding layer*, which converts the final vector representations back to a probability distribution over the tokens.

i) Tokenizers. As illustrated in Fig. 2(a), the input to the BDT model consists of a set of N independent R - t curves. Each curve is represented as a sequence of 100 discrete bubble radius data points, for example, it can be $\{R_1, \dots, R_{100}\}$ that are sampled at 100 uniformly spaced time points over an 80 μ s interval with a temporal resolution of 0.8 μ s. These curves are collected from different simulations and serve as the foundation for the model to learn from.

ii) Embedding layer. Each token is converted into an embedding vector via a lookup table¹⁴. Each of the 100

input radius values is concatenated with a corresponding 64-dimensional positional embedding that encodes its precise location in the temporal sequence¹⁴. To help the model understand not just the size of the bubble at each moment but also when that moment occurs in the sequence, we use a technique called positional encoding. A positional encoding is a fixed-size vector representation of the relative positions of tokens within a sequence: it provides the transformer model with information about where the data are in the input sequence. This means that each of the 100 radius values is combined with information about its exact position in the timeline. This added information allows the model to distinguish between early and late stages of the collapse, which is crucial for learning the correct patterns. These embeddings are generated via a learnable embedding layer that maps positional indices to continuous representations¹⁴. The combined input—comprising both the raw radius values and their associated positional encodings—is subsequently passed through a nonlinear projection implemented via a dense layer with *softplus* activation²⁹, followed by layer normalization (where parameter $\epsilon = 10^{-6}$ serves as a small constant ensuring numerical stability) and dropout regularization (rate = 0.1) to enhance training stability and mitigate overfitting³⁰.

iii) Transformer layers. After preparing the input data, we feed it into the heart of the model: the Transformer encoder (see Fig. 2(c)). Originally developed for language processing (like translating text), the Transformer is very good at recognizing patterns over sequences. It uses a multi-head self-attention mechanism to effectively capture temporal dependencies and long-range interactions inherent in bubble dynamics^{31,32}, which helps the model look at different parts of the time sequence at once and figure out how they relate to each other. For example, it can learn that a sudden decrease in radius is often followed by a rebound, and how these changes relate to the stiffness or viscosity of the material.

The attention mechanism works by turning each time step in the sequence into three mathematical objects—query (\mathbf{Q}), key (\mathbf{K}), and value (\mathbf{V})—and computing how much attention each part of the sequence should pay to every other part (see Fig. 2(d)). This helps the model focus on the most important moments in the bubble’s behavior.

After the multi-head self-attention step, the encoder employs residual connections and layer normalization (Add & Norm) to enhance training stability and facilitate efficient gradient propagation³³. A position-wise feed-forward neural network further refines the encoded features, followed by an additional normalization step to consolidate the learned representations.

iv) Un-embedding layer. At the end of the process, the model uses global average pooling to summarize the full sequence into a single, compact set of features. These features are then passed through final layers that produce the predicted microrheology properties, such as the shear modulus (G) and viscosity (μ) in the neo-Hookean Kelvin-Voigt (NHKV) material model.

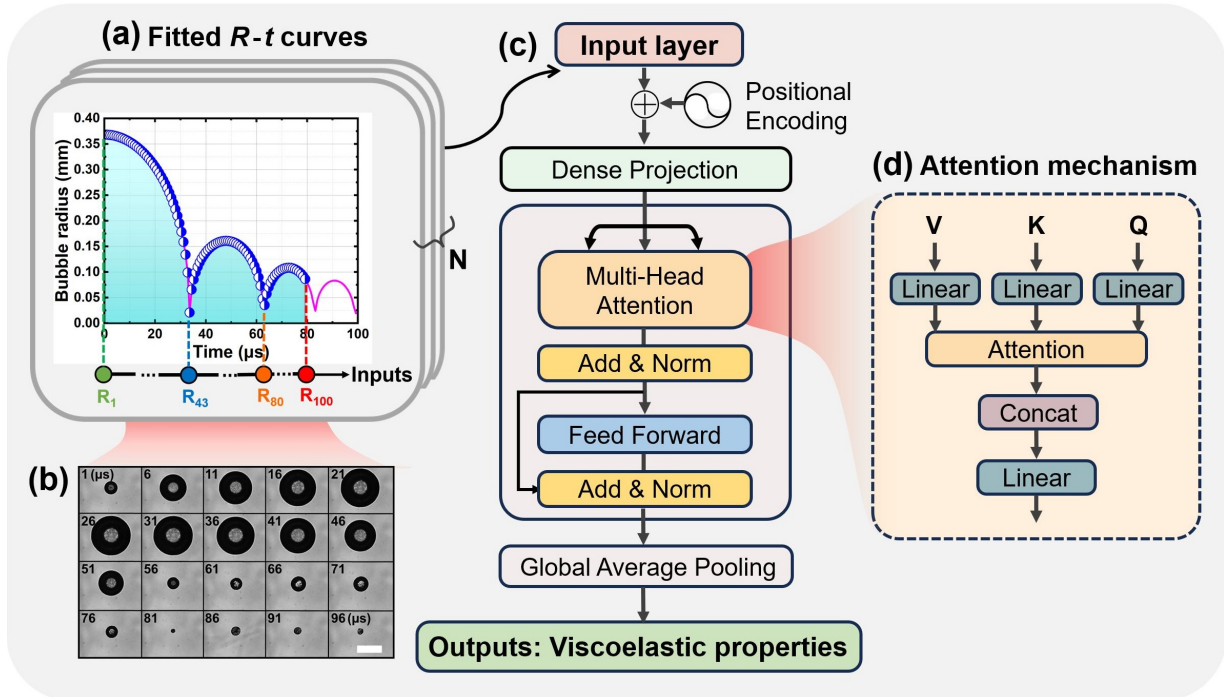


FIG. 2. Schematic overview of the Bubble Dynamics Transformer (BDT) model for predicting viscoelastic properties of soft materials. (a) The model input consists of N independent bubble radius versus time (R vs t) curves. (b) Selected frames in a typical laser-induced inertial cavitation event in a PAAm 12% hydrogel (scale bar: 500 μm). (c) Each curve is passed through an input layer with positional encoding, followed by a dense projection, Transformer encoder blocks with multi-head self-attention, and a global average pooling layer. (d) Within the attention block, the input sequence is transformed into query (Q), key (K), and value (V) matrices to compute temporal dependencies. The model outputs are the predicted viscoelastic parameters: shear modulus (G) and viscosity (μ).

D. Simulated Training Data for Bubble Dynamics Transformer (BDT)

To train the BDT model, we synthetically generated a dataset using our previously developed Inertial Microcavitation Rheometry (IMR) numerical simulation code²². These simulations utilized the neo-Hookean Kelvin-Voigt (NHKV) constitutive model, which represents the surrounding material as a neo-Hookean hyperelastic spring in parallel with a linear viscous dashpot. For all simulations, the material stiffening parameter (α) was fixed at zero.

We sampled the shear modulus (G) and viscosity (μ) from uniformly random distributions in logarithmic space: specifically, $\log_{10}(G) \in [3, 6]$ (unit: Pa) and $\log_{10}(\mu) \in [-3, 0]$ (unit: Pa·s). To introduce variability in the collapse dynamics, the maximum bubble expansion ratio, $\lambda = R_{\max}/R_0$, was also sampled uniformly at random from the range [6, 11]. These ranges were chosen based on our experience from previously tested soft materials and from data observed in a wide range of soft materials^{6-9,11,13,21,22,34,35} from soft hydrogel/tissue to relatively stiffer elastomers. Using these parameters, we simulated a total of 16,335 distinct bubble dynamics where each generated R vs t curve uses a randomly selected parameter set $\{G, \mu, \lambda\}$ within the above specified ranges.

Each simulation generated a bubble radius-versus-time curve, $R(t)$, sampled at 100 evenly spaced time points over an 80 μs interval (temporal resolution of 0.8 μs). These $R(t)$

curves were used as the input features for training the BDT model, while the corresponding $\log(G)$ and $\log(\mu)$ values served as the target outputs.

E. Training and validation

The BDT model utilizes *softplus* activation functions throughout the network and incorporates residual connections with layer normalization (with parameter $\epsilon = 1 \times 10^{-6}$) to facilitate stable gradient flow. Training was performed over 100 epochs with a batch size of 32 using the Adam optimizer (learning rate = 0.001) and a mean squared error (MSE) loss function:

$$\text{MSE} = \frac{1}{N} \sum_{i=1}^N (\hat{y}_i - y_i)^2 \quad (5)$$

where N is the total number of data points, y_i is the ground truth value for the i -th data, and \hat{y}_i is the corresponding predicted value.

To ensure effective model training, 80% of the dataset was used for training, with 10% allocated for validation. As shown in Fig. 3(a) and (b), the model demonstrated convergence for both $\log(G)$ and $\log(\mu)$ within 100 training epochs. The remaining 10% of the dataset was reserved for

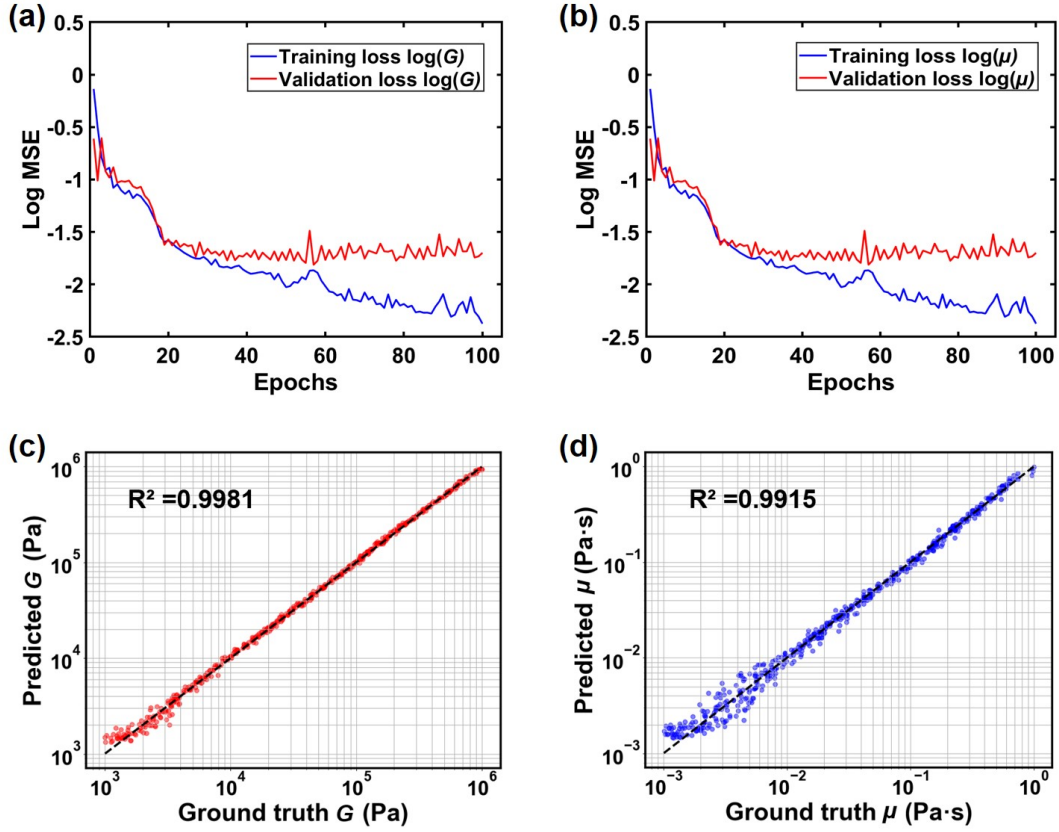


FIG. 3. Training and validation performance of the Bubble Dynamics Transformer (BDT) model. (a, b) Training and validation loss curves for $\log(G)$ and $\log(\mu)$, respectively, showing convergence over 100 epochs. (c, d) Predicted versus ground truth values of shear modulus G and viscosity μ on the synthetic test set, demonstrating excellent agreement with $R^2 = 0.9981$ and $R^2 = 0.9915$, respectively.

testing the model's predictive performance by comparing the predicted values of G and μ against their corresponding ground truth values. The coefficient of determination (R^2) can be employed as the evaluation metric³⁶. As illustrated in Fig. 3(c) and (d), the R^2 values for the predicted ground-state shear modulus (G) and viscosity (μ) are 0.9981 and 0.9915, respectively, indicating excellent agreement with the ground truth and demonstrating the high accuracy of the model in capturing material properties.

III. RESULTS

To assess the predictive capabilities of the Bubble Dynamics Transformer (BDT) model, we applied it to experimental data from laser-induced cavitation (LIC) in 12% polyacrylamide (PAAm) hydrogels. These hydrogels were prepared with varying Alginate concentrations: 0%, 0.3%, 0.6%, 1.0%, 1.3%, and 2.0% (see Section II A “Experimental Setup”). Figure 4 illustrates the normalized bubble radius dynamics (R^*) as a function of non-dimensional time (t^*) for six representative samples, one for each Alginate concentration. Each subfigure in Fig. 4 compares the experimental measurements

(dotted lines) with predictions from the conventional Inertial Microcavitation Rheology (IMR) model (solid lines) and our proposed BDT model (dashed lines). Across all tested Alginate concentrations, the bubble dynamics predicted by the BDT model demonstrate a very close agreement with the experimental trends compared to the IMR model for 0%-1.0% alginate concentrations.

A quantitative comparison of the shear modulus (G ; also storage modulus) and viscosity (μ) extracted using the BDT, IMR, and classic quasi-static uniaxial tensile testing is presented in Table I. The BDT model demonstrated high accuracy in predicting the shear modulus (G), with relative errors remaining below 15% for all samples with Alginate concentrations up to 1.0%. However, the most significant discrepancies in G estimation were observed for samples with 1.3% and 2.0% Alginate (93.8% and 137.2% error, respectively). This increase in error at higher Alginate concentrations is likely due to material stiffening and the emergence of other mechanical responses, such as fracture and plasticity, which deviate from the viscoelastic behavior predominantly represented in the model's training distribution. Comparing the high-rate methods (BDT and IMR) against the quasi-static tensile tests revealed significant rate-dependent stiffening. For the hydrogel with 0% alginate, the shear modulus measured

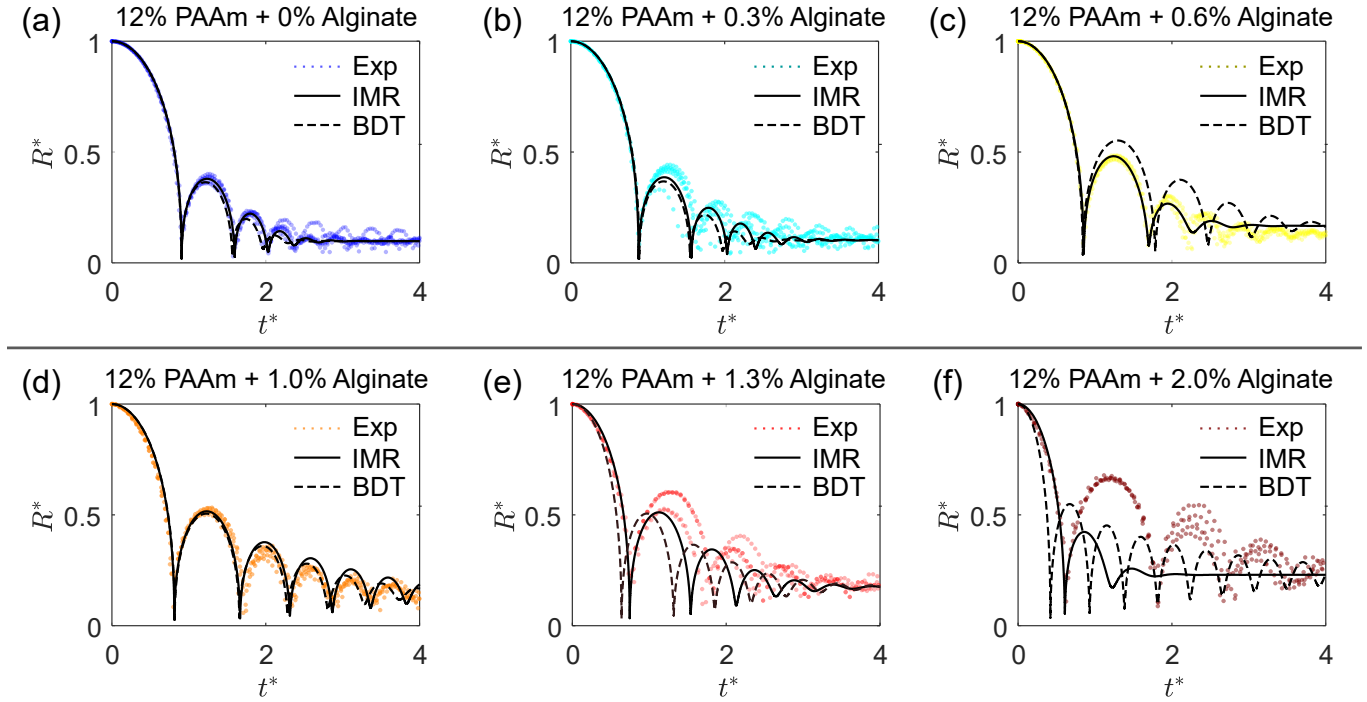


FIG. 4. Experimental demonstrations of viscoelastic property prediction using the Bubble Dynamics Transformer (BDT). (a-f) Comparison of normalized bubble radius dynamics (R^* vs. t^*) for 12% PAAm hydrogels with increasing Alginate concentrations (0% to 2.0%). Experimental data (dotted lines), Inertial Microcavitation Rheometry (IMR) predictions (solid lines), and BDT model predictions (dashed lines) are shown. The BDT model demonstrates improved agreement with experimental bubble dynamics across a range of stiffness and damping regimes. Material parameters extracted from BDT and IMR are summarized in Table I, showing that BDT achieves lower relative errors in shear modulus G for most cases, despite using only R_{\max} and collapse time t_c as input features.

TABLE I. Estimated viscoelastic material properties using only collapse time t_c and the maximum bubble radius (R_{\max}) in LIC experiments

Alginate %	Method	G (kPa)	μ (Pa·s)	Relative error G	Relative error μ
0%	LIC test: IMR	4.20 ± 1.21	0.0418 ± 0.0082	—	—
	LIC test: BDT	4.83 ± 0.81	0.0553 ± 0.0078	15.0 %	32.3 %
	Quasistatic, tensile test	0.55	—	86.9%	—
0.3%	LIC test: IMR	6.44 ± 1.64	0.0203 ± 0.0093	—	—
	LIC test: BDT	5.94 ± 1.03	0.0345 ± 0.0100	7.7%	70.0%
	Quasistatic, tensile test	3	—	53.4%	—
0.6%	LIC test: IMR	13.82 ± 0.91	0.0954 ± 0.0186	—	—
	LIC test: BDT	13.29 ± 1.72	0.0414 ± 0.0075	3.8%	56.6%
	Quasistatic, tensile test	8	—	42.1%	—
1.0%	LIC test: IMR	15.71 ± 1.18	0.0077 ± 0.0037	—	—
	LIC test: BDT	15.43 ± 1.13	0.0144 ± 0.0030	1.8%	87.0%
	Quasistatic, tensile test	20	—	27.3%	—
1.3%	LIC test: IMR	29.71 ± 3.49	0.0361 ± 0.0439	—	—
	LIC test: BDT	57.58 ± 1.02	0.0245 ± 0.0018	93.8%	32.1%
	Quasistatic, tensile test	25.8	—	13.2%	—
2.0%	LIC test: IMR	85.81 ± 5.43	0.1281 ± 0.0477	—	—
	LIC test: BDT	203.58 ± 36.77	0.0041 ± 0.0013	137.2%	96.8%
	Quasistatic, tensile test	50	—	41.7%	—

at high strain rates was approximately one order of magnitude greater than its quasi-static value. In contrast, for hydrogels with higher alginate concentrations, this rate-stiffening effect was less pronounced, with the high-rate shear moduli being only 1-2 times greater than the values obtained from low-rate

tests.

Consistent with expectations and observations from conventional IMR analyses²², the prediction errors for viscosity (μ) were generally higher than those for the shear modulus (G) across all samples. This is as expected due to the reduced

sensitivity of the resulting bubble $R - t$ curve during the first violent collapse regime to the viscous effects.

Computational Costs

The BDT model was implemented in Python 3.10 using TensorFlow 2.0 and trained on an NVIDIA GeForce GTX 4070Ti GPU platform.

All dataset generation processes were conducted using MATLAB (version 2023b, 64-bit) on a workstation equipped with an Intel Core i7-13700KF CPU (3.40 GHz base clock, 24 threads), 64 GB of memory, and running Windows 10. The generation of the dataset, comprising 16,355 $R(t)$ curves, utilized 24 computational threads through Matlab's Parallel Computing Toolbox and was completed in approximately one week.

The Bubble Dynamics Transformer (BDT) model was trained in approximately 10 minutes using an NVIDIA GeForce GTX 4070Ti GPU. Once trained, the model facilitates rapid inference of viscoelastic material properties. Specifically, the average prediction times for 12% PAAm hydrogels with increasing alginate concentrations (from 0% to 2.0%) reported in Table I were 0.613, 0.658, 0.617, 0.606, 0.616, and 0.639 seconds, respectively.

IV. CONCLUSIONS

This work addressed the need for rapid material characterization at high strain rates by developing a novel deep-learning framework to augment the inertial microcavitation rheometry (IMR) method. IMR is a recently established technique for extracting soft material properties at ultra-high strain rates ($> 10^3 \text{ s}^{-1}$) by analyzing inertial cavitation dynamics. To significantly accelerate the data processing aspect of IMR for potential real-time applications, we introduced the Bubble Dynamics Transformer (BDT) model, specifically designed to infer the viscoelastic properties of hydrogels using minimal experimental inputs.

The BDT architecture demonstrated robust training behavior and high predictive accuracy across a wide range of material stiffness and damping conditions. Critically, when compared against conventional physics-based IMR fitting procedures, the BDT model leverages the entire normalized radius-time curve ($R(t)$) from experiments to predict the shear modulus (G) and viscosity (μ) of the surrounding medium. While utilizing the same comprehensive input data as traditional full-curve IMR fitting, the BDT model achieves comparable accuracy in estimating viscoelastic material properties, with the significant advantage of notably improved processing speed once trained.

However, for soft materials exhibiting highly nonlinear phenomena such as material fracture or plasticity during cavitation experiments, both conventional IMR (especially when reliant on simpler constitutive models like the Kelvin-Voigt

model) and the current BDT model may struggle to accurately capture the bubble dynamics. This is because such complex behaviors often deviate from the assumptions underlying standard viscoelastic models. Incorporating material failure and damage mechanisms into the underlying bubble dynamics theory and, consequently, into the BDT model's training paradigm, remains a key area for future investigation.

In summary, the successful development and application of the BDT framework underscore its potential as a powerful tool for rapid, data-driven characterization of soft viscoelastic materials by analyzing their complete bubble dynamics profiles. This approach promises to open new pathways for high-throughput, non-invasive diagnostics in diverse fields, including soft tissue mechanics, hydrogel development, and biomedical device evaluation. Future extensions of this work may focus on incorporating uncertainty quantification, expanding the training datasets to encompass an even broader spectrum of material responses and experimental conditions, and deploying the BDT model for real-time, *in situ* material assessment.

ACKNOWLEDGMENT

We gratefully acknowledge support by the U.S. National Science Foundation (NSF) under Grant No. 2232428 and 2441460. J.Y. acknowledges the start-up fund from the University of Texas at Austin, the Haythornthwaite Foundation for the Research Initiation Grant awarded by the Applied Mechanics Division of the American Society of Mechanical Engineers (ASME).

Appendix A: Bubble Contents Dynamics

This appendix summarizes the governing equations for the physics of the bubble contents based on established literature concerning laser-induced cavitation bubbles^{6,25–27}, with a more comprehensive discussion available in Estrada *et al.*⁶. We model the bubble internal contents as a homobaric (uniform pressure), two-phase mixture of water vapor and a non-condensable gas, both treated as ideal gases. The evolution of the (dimensionless) vapor mass fraction field, $k(r,t)$, and the temperature field, $T(r,t)$, inside the bubble ($(0 \leq r \leq R)$) are governed by:

$$\frac{\partial k}{\partial t} + v_m \frac{\partial k}{\partial r} = \frac{1}{\rho_m r^2} \frac{\partial}{\partial r} \left(\rho_m r^2 D \frac{\partial k}{\partial r} \right) \quad (\text{A1})$$

and

$$\frac{\kappa}{\kappa - 1} \frac{p_b}{T} \left(\frac{\partial T}{\partial t} + v_m \frac{\partial T}{\partial r} \right) = \dot{p}_b + \frac{1}{r^2} \frac{\partial}{\partial r} \left(r^2 K \frac{\partial T}{\partial r} \right) + \frac{\kappa}{\kappa - 1} \frac{p_b}{T} \frac{\mathcal{R}_v - \mathcal{R}_g}{\mathcal{R}} D \frac{\partial k}{\partial r} \frac{\partial T}{\partial r}, \quad (\text{A2})$$

In these equations, $v_m(r,t)$ is the mixture velocity:

$$v_m(r,t) = \frac{1}{\kappa p_b} \left[(\kappa - 1) K \frac{\partial T}{\partial r} - \frac{1}{3} r \dot{p}_b \right] + \frac{\mathcal{R}_v - \mathcal{R}_g}{\mathcal{R}} D \frac{\partial k}{\partial r}; \quad (\text{A3})$$

TABLE II. Parameters describing the physics of the bubble contents

Parameter	Value	Parameter	Value
D	$24.2 \times 10^{-6} \text{ m}^2/\text{s}$	κ	1.4
\mathcal{R}_v	0.462 kJ/kg·K	\mathcal{R}_g	0.287 kJ/kg·K
A	$5.3 \times 10^{-5} \text{ W/m}\cdot\text{K}^2$	B	$1.17 \times 10^{-2} \text{ W/m}\cdot\text{K}$
p_{ref}	$1.17 \times 10^8 \text{ kPa}$	T_{ref}	5200 K
T_{∞}	298.15 K		

$\rho_m = p_b/\mathcal{R}T$ is the mixture density field, $\mathcal{R} = k\mathcal{R}_v + (1-k)\mathcal{R}_g$ is the mixture gas constant field, and $K(T) = AT + B$ is the temperature-dependent thermal conductivity of the mixture³⁷, where A and B are empirical constants. The gas constants for water vapor and non-condensable gas are \mathcal{R}_v and \mathcal{R}_g , respectively. The evolution of the bubble pressure $p_b(t)$ is described by the ordinary differential equation:

$$\dot{p}_b = \frac{3}{R} \left[-\kappa p_b \dot{R} + (\kappa - 1)K(T|_{r=R}) \frac{\partial T}{\partial r} \Big|_{r=R} + \kappa p_b \frac{\mathcal{R}_v}{\mathcal{R}(k|_{r=R})} \frac{D}{1-k|_{r=R}} \frac{\partial k}{\partial r} \Big|_{r=R} \right]. \quad (\text{A4})$$

The constant parameters governing the bubble contents—including the binary diffusion coefficient (D), the specific heat ratio (κ), gas constants ($\mathcal{R}_v, \mathcal{R}_g$), and empirical thermal conductivity constants (A, B)—are summarized in Table II.

Boundary and Initial Conditions:

At the bubble center ($r = 0$), we apply symmetry boundary conditions: $\partial T/\partial r|_{r=0} = \partial k/\partial r|_{r=0} = 0$. At the bubble wall ($r = R$), we assume the surrounding medium is cold and isothermal, imposing the boundary condition $T|_{r=R} = T_{\infty}$. The partial pressure of the water vapor at the wall is assumed to equal its saturation pressure, yielding the following boundary condition for the vapor mass fraction:

$$k|_{r=R} = \left[1 + \frac{\mathcal{R}_v}{\mathcal{R}_g} \left(\frac{p_b}{p_{v,\text{sat}}(T_{\infty})} - 1 \right) \right]^{-1}, \quad (\text{A5})$$

where $p_{v,\text{sat}}(T) = p_{\text{ref}} \exp(-T_{\text{ref}}/T)$ is the temperature-dependent saturation pressure of the water vapor with empirical constants p_{ref} and T_{ref} ²⁷. Quantitative values for p_{ref} , T_{ref} , and T_{∞} used in this study are included in Table II.

For the initial conditions ($t = 0$), we assume the bubble contents are in thermal equilibrium. The initial temperature is therefore uniform at the ambient temperature, $T(r, t = 0) = T_{\infty}$. Consequently, the initial vapor mass fraction, $k(r, t = 0)$, is also spatially uniform and given by Eq. (A5). Following Estrada *et al.*⁶, the initial bubble pressure for LIC is given by:

$$p_b(t = 0) = p_{v,\text{sat}}(T_{\infty}) + \left(p_{\infty} + \frac{2\gamma}{R_0} - p_{v,\text{sat}}(T_{\infty}) \right) \left(\frac{R_0}{R_{\max}} \right)^3. \quad (\text{A6})$$

Numerical Implementation:

For the numerical solution, the governing equations are first non-dimensionalized as detailed in Estrada *et al.*⁶. The spatial domain within the bubble is discretized onto a grid of $N +$

$1 = 501$ equidistant points. Spatial derivatives in Eqs. (A1) and (A2) are then approximated using second-order central differences³⁷. The resulting system of ordinary differential equations is evolved forward in time, in conjunction with the Keller-Miksis equation, using a variable-step, variable-order solver (MATLAB's `ode15s`).

REFERENCES

- C. E. Brennen, "Cavitation in medicine," *Interface Focus* **5**, 20150022 (2015).
- K. Hyun, M. Wilhelm, C. O. Klein, K. S. Cho, J. G. Nam, K. H. Ahn, S. J. Lee, R. H. Ewoldt, and G. H. McKinley, "A review of nonlinear oscillatory shear tests analysis and application of large amplitude oscillatory shear (laos)," *Progress in Polymer Science* **36**, 1697–1753 (2011).
- R. P. Chartoff, J. D. Menczel, and S. H. Dillman, "Dynamic mechanical analysis (dma)," *Thermal Analysis of Polymers Fundamentals and Applications*, 387–495 (2009).
- Y. F. Dufrêne, "Towards nanomicrobiology using atomic force microscopy," *Nature Reviews Microbiology* **6**, 674–680 (2008).
- W. C. Oliver and G. M. Pharr, "Nanoindentation in materials research past, present, and future," *MRS Bulletin* **35**, 897–907 (2010).
- J. B. Estrada, C. Barajas, D. L. Henann, E. Johnsen, and C. Franck, "High strain-rate soft material characterization via inertial cavitation," *Journal of the Mechanics and Physics of Solids* **112**, 291–317 (2018).
- J. Yang, H. C. Cramer, and C. Franck, "Extracting non-linear viscoelastic material properties from violently-collapsing cavitation bubbles," *Extreme Mechanics Letters* **39**, 100839 (2020).
- J. Yang, H. C. Cramer III, E. C. Bremer, S. Buyukozturk, Y. Yin, and C. Franck, "Mechanical characterization of agarose hydrogels and their inherent dynamic instabilities at ballistic to ultra-high strain-rates via inertial microcavitation," *Extreme Mechanics Letters* **51**, 101572 (2022).
- J. Yang, A. McGhee, G. Radtke, M. Rodriguez, and C. Franck, "Estimating viscoelastic, soft material properties using a modified rayleigh cavitation bubble collapse time," *Physics of Fluids* **36** (2024).
- Z. Zhu, S. Remillard, B. A. Abeid, D. Frolikin, S. H. Bryngelson, J. Yang, M. Rodriguez, and J. Estrada, "Parsimonious inertial cavitation rheometry via bubble collapse time," Available at SSRN 5098460 (2025).
- L. Mancia, J. Yang, J.-S. Spratt, J. R. Sukovich, Z. Xu, T. Colonius, C. Franck, and E. Johnsen, "Acoustic cavitation rheometry," *Soft Matter* **17**, 2931–2941 (2021).
- C. T. Wilson, T. L. Hall, E. Johnsen, L. Mancia, M. Rodriguez, J. E. Lundt, T. Colonius, D. L. Henann, C. Franck, and Z. Xu, "Comparative study of the dynamics of laser and acoustically generated bubbles in viscoelastic media," *Physical Review E* **99**, 043103 (2019).
- A. McGhee, J. Yang, E. Bremer, Z. Xu, H. Cramer III, J. Estrada, D. Henann, and C. Franck, "High-speed, full-field deformation measurements near inertial microcavitation bubbles inside viscoelastic hydrogels," *Experimental Mechanics* **63**, 63–78 (2023).
- A. Vaswani, N. Shazeer, N. Parmar, J. Uszkoreit, L. Jones, A. N. Gomez, L. Kaiser, and I. Polosukhin, "Attention is all you need," *Advances in Neural Information Processing Systems* **30** (2017).
- B. Saint-Michel and V. Garbin, "Acoustic bubble dynamics in a yield-stress fluid," *Soft Matter* **16**, 10405–10418 (2020).
- K. Murakami, Y. Yamakawa, J. Zhao, E. Johnsen, and K. Ando, "Ultrasound-induced nonlinear oscillations of a spherical bubble in a gelatin gel," *Journal of Fluid Mechanics* **924**, A38 (2021).
- S. Lin, C. D. Londono, D. Zheng, and X. Zhao, "An extreme toughening mechanism for soft materials," *Soft Matter* **18**, 5742–5749 (2022).
- L. Mancia, M. Rodriguez, J. R. Sukovich, S. Haskell, Z. Xu, and E. Johnsen, "Acoustic measurements of nucleus size distribution at the cavitation threshold," *Ultrasound in Medicine & Biology* **47**, 1024–1031 (2021).
- A. D. Maxwell, C. A. Cain, T. L. Hall, J. B. Fowlkes, and Z. Xu, "Probability of cavitation for single ultrasound pulses applied to tissues and tissue-mimicking materials," *Ultrasound Med. Biol.* **39**, 449–465 (2013).
- J. R. Sukovich, S. C. Haskell, Z. Xu, and T. L. Hall, "A cost-effective, multi-flash, "ghost" imaging technique for high temporal and spatial reso-

lution imaging of cavitation using “still-frame” cameras,” *J. Acoust. Soc. Am.* **147**, 1339–1343 (2020).

²¹J. Yang and C. Franck, “Strain stiffening effects of soft viscoelastic materials in inertial microcavitation,” in *Dynamic Behavior of Materials, Volume 1 Proceedings of the 2019 Annual Conference on Experimental and Applied Mechanics* (Springer, 2019) pp. 175–179.

²²A. Tzoumaka, J. Yang, S. Buyukozturk, C. Franck, and D. L. Henann, “Modeling high strain-rate microcavitation in soft materials the role of material behavior in bubble dynamics,” *Soft Matter* **19**, 3895–3909 (2023).

²³Y. Mao, S. Lin, X. Zhao, and L. Anand, “A large deformation viscoelastic model for double-network hydrogels,” *Journal of the Mechanics and Physics of Solids* **100**, 103–130 (2017).

²⁴R. Gaudron, M. T. Warnez, and E. Johnsen, “Bubble dynamics in a viscoelastic medium with nonlinear elasticity,” *Journal of Fluid Mechanics* **766**, 54–75 (2015).

²⁵R. Nigmatulin, N. Khabeey, and F. Nagiev, “Dynamics, heat and mass transfer of vapour-gas bubbles in a liquid,” *International Journal of Heat and Mass Transfer* **24**, 1033–1044 (1981).

²⁶I. Akhatov, O. Lindau, A. Topolnikov, R. Mettin, N. Vakhitova, and W. Lauterborn, “Collapse and rebound of a laser-induced cavitation bubble,” *Physics of Fluids* **13**, 2805 (2001).

²⁷C. Barajas and E. Johnsen, “The effects of heat and mass diffusion on freely oscillating bubbles in a viscoelastic, tissue-like medium,” *The Journal of the Acoustical Society of America* **141**, 908–918 (2017).

²⁸S. Hochreiter and J. Schmidhuber, “Long short-term memory,” *Neural computation* **9**, 1735–1780 (1997).

²⁹X. Glorot, A. Bordes, and Y. Bengio, “Deep sparse rectifier neural networks,” in *Proceedings of the fourteenth international conference on artificial intelligence and statistics* (JMLR Workshop and Conference Proceedings, 2011) pp. 315–323.

³⁰M. Kowsher, A. A. Sami, N. J. Prottasha, M. S. Arefin, P. K. Dhar, and T. Koshiba, “Bangla-bert transformer-based efficient model for transfer learning and language understanding,” *IEEE Access* **10**, 91855–91870 (2022).

³¹J. Liu, S. Chen, B. Wang, J. Zhang, N. Li, and T. Xu, “Attention as relation learning supervised multi-head self-attention for relation extraction,” in *Proceedings of the twenty-ninth international conference on international joint conferences on artificial intelligence* (2021) pp. 3787–3793.

³²S. Ahmed, I. E. Nielsen, A. Tripathi, S. Siddiqui, R. P. Ramachandran, and G. Rasool, “Transformers in time-series analysis: A tutorial,” *Circuits, Systems, and Signal Processing* **42**, 7433–7466 (2023).

³³J. Xu, X. Sun, Z. Zhang, G. Zhao, and J. Lin, “Understanding and improving layer normalization,” *Advances in Neural Information Processing Systems* **32** (2019).

³⁴J. Yang, A. Tzoumaka, K. Murakami, E. Johnsen, D. L. Henann, and C. Franck, “Predicting complex nonspherical instability shapes of inertial cavitation bubbles in viscoelastic soft matter,” *Physical Review E* **104**, 045108 (2021).

³⁵E. Bremer-Sai, J. Yang, A. McGhee, and C. Franck, “Ballistic and blast-relevant, high-rate material properties of physically and chemically crosslinked hydrogels,” *Experimental Mechanics* **64**, 587–592 (2024).

³⁶A. E. Allen and A. Tkatchenko, “Machine learning of material properties predictive and interpretable multilinear models,” *Science Advances* **8**, eabm7185 (2022).

³⁷A. Prosperetti, L. A. Crum, and K. W. Commander, “Nonlinear bubble dynamics,” *J. Acoust. Soc. Am.* **83**, 502–514 (1988).